ROYAL SOCIETY
OF CHEMISTRY

PAPER

Check for updates

Construction of polypyrrole nanoparticles with a rough surface for enhanced chemo-photothermal therapy against triple negative breast cancer†

Yuanyin Xi,‡[a] Shiqi Zhou,‡[b] Junhui Long,[c] Linxi Zhou,[a] Peng Tang,[a] Hang Qian, [iD]*[d] Jun Jiang*[a] and Ying Hu*[a]

Triple-negative breast cancer (TNBC) is the most malignant subtype of breast cancer, characterized by aggressive malignancy and a poor prognosis. Emerging nanomedicine-based combination therapy represents one of the most promising strategies for combating TNBC. Polypyrrole nanoparticles (PPY) are excellent drug delivery vehicles with outstanding photothermal performances. However, the impact of morphology on PPY's drug loading efficiency and photothermal properties remains largely unexplored. In this study, we propose that pluronic P123 can assist in the synthesis of polypyrrole nanoparticles with rough surfaces (rPPY). During the synthesis, P123 formed small micelles around the nanoparticle surface, which were later removed, resulting in small pits and cavities in rPPY. Subsequently, the rPPY was loaded with the chemotherapy drug gemcitabine (Gem@rPPY) for chemo-photothermal therapy against TNBCs. Our results demonstrate that rPPY exhibited superior photothermal performance and significantly enhanced drug loading efficiency by five times compared to smooth PPY nanoparticles. *In vitro* assessments confirmed Gem@rPPY's robust photothermal properties by efficiently converting light into heat. Cell culture experiments with 4T1 cells and a TNBC mice model revealed significant tumor suppression upon Gem@rPPY administration, emphasizing its efficacy in inducing apoptosis. Toxicity evaluations demonstrated minimal adverse effects both *in vitro* and *in vivo*, highlighting the biocompatibility of Gem@rPPY. Overall, this study introduces a promising combination therapy nanoplatform that underscores the importance of surface engineering to enhance therapeutic outcomes and overcome current limitations in TNBC therapy.

1. Introduction

Breast cancer, particularly triple-negative breast cancer (TNBC), represents a formidable challenge in oncology, ranking as the second leading cause of cancer-related deaths in women, according to recent data from the American Cancer Society.[1,2] TNBC is a distinct and aggressive subtype of breast cancer, characterized by the absence of human epidermal growth factor receptor 2 (HER2), progesterone receptors, and estrogen receptors (ER) on the cancer cell surfaces.[3–7] Comprising 20% of all breast cancers, TNBC is associated with heightened malignancy, poor prognosis, and increased mortality due to the lack of well-established targeted and endocrine therapies.[8–10] Traditional TNBC treatment options, including surgery and chemotherapy with anthracyclines, paclitaxel, and antimetabolites, have limitations such as significant toxicity and drug resistance.[11–13] Recognizing the high metabolic activity of tumor cells, which leads to an accumulation of hydrogen peroxide (H_2O_2) and reduced glutathione (GSH), researchers have explored novel approaches, including photothermal therapies (PTTs).[14,15] It has been suggested that, besides the direct killing effect on cancer cells, heat stress can also boost the consumption of reduced GSH and the conversion of H_2O_2 to highly cytotoxic ROS through Fenton reactions.[16–18] The ensuing apoptosis resulting from this process contributes significantly to the effective suppression of tumor growth.[19] Given the considerable risks associated with posttreatment side effects and the limitations of traditional therapies,[20,21] there has been a surge in the development of PTTs. PTTs focus on converting

[a] *Breast Disease Center, Southwest Hospital, Army Medical University, Chongqing 400038, China. E-mail: totoyingying@hotmail.com; a_jiangjun001@163.com*

[b] *Department of Plastic, Reconstructive and Cosmetic Surgery, Xinqiao Hospital, Army Medical University, Chongqing 400037, China*

[c] *Department of Dermatology, The 958th Army Hospital of the Chinese People's Liberation Army, China*

[d] *Department of Respiratory and Critical Care Medicine, Second Affiliated Hospital of Army Medical University, Chongqing 400037, China. E-mail: hqian@tmmu.edu.cn*

† Electronic supplementary information (ESI) available. See DOI: https://doi.org/10.1039/d4na00434e
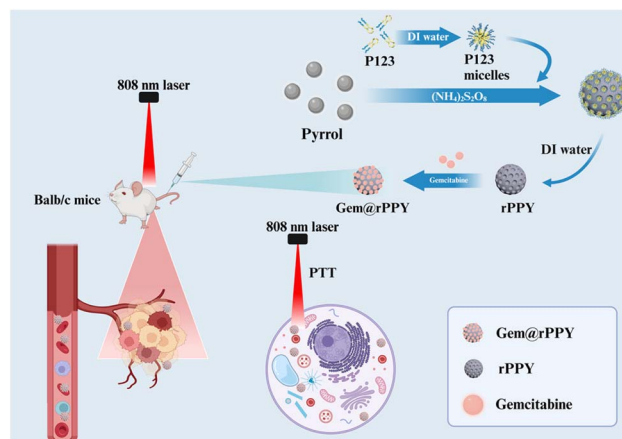
‡ These authors contributed equally to this work.

absorbed light into heat energy through photothermal agents (PTAs), such as gold-based nanoparticles, carbon nanotubes, and CuxSy.[22–27] Notably, various metals, including upconversion nanostructures, copper, and gold, have been widely utilized due to their near-infrared (NIR) absorption capabilities.[28] These advancements in PTTs hold promise for overcoming the challenges posed by conventional treatments and offer a potential avenue for more effective cancer therapy.

However, the intricate and demanding chemical procedures involved in the preparation of upconversion nanoparticles and gold come with substantial financial and time costs. Moreover, the application of metal nanoparticles is constrained by potential toxicity concerns, as they can persist in the body for extended periods.[24] Despite their ability to noninvasively eliminate solid tumors under hypoxic tumor microenvironments and spare normal cells from damage, PTTs face limitations, including incomplete tumor removal and significant tumor relapse due to heat endurance.[29–33] Recognizing these challenges, recent research indicates that relying solely on a single therapeutic modality may not suffice to achieve optimal clinical outcomes, prompting the exploration of multifaceted approaches to enhance treatment efficacy.[27,34–36]

To address these issues, recent studies have highlighted the promise of polypyrrole nanoparticles (PPY NPs) as a photothermal agent due to their broad near-infrared (NIR) absorption spectrum, efficient light energy conversion, and straightforward synthesis.[37,38] The synthesis of various PPY NPs often involves the use of surfactants such as polyvinylpyrrolidone (PVP) and polyvinyl alcohol (PVA). The presence of surfactants significantly influences the synthesis of PPY nanoparticles by stabilizing the growth process, controlling particle size and morphology, enabling surface functionalization, and enhancing solubility.[39] It has been reported that the nanostructures of nanoparticles play a crucial role in determining their photothermal capabilities and drug loading efficiency.[40,41] The most common form of polypyrrole nanomaterials consists of spherical nanoparticles with diameters typically in the range of dozens of nanometers. A few studies have focused on developing PPY nanomaterials with different shapes and morphologies. Qiu *et al.* reported the successful creation of PPY nanorings through direct chemical oxidative polymerization reactions.[42] These nanorings exhibited significantly enhanced photothermal conversion performance and demonstrated additional properties such as shape memory, reshaping, and welding. Another study found that PPY composite nanoparticles with a raspberry-like morphology displayed improved photothermal effects possibly due to their taper-like surface structure.[43] These investigations underscore the importance of the nanostructures and surface properties of PPY nanomaterials in influencing their photothermal performance. However, there is limited reported research on the engineering of PPY nanostructures and surface morphology.

In this study, we present a pioneering study focused on designing and synthesizing polypyrrole nanoparticles with roughed surfaces (rPPY). As shown in Scheme 1, a block copolymer, pluronic P123 is proposed as the soft template to control the surface morphology of polypyrrole nanoparticles.

Scheme 1 Design and workflow diagram of Gem@rPPY.

The micelle structure of P123 acts as a template during the curing process. Gemcitabine, a widely used chemotherapy drug, was encapsulated in the polypyrrole nanoparticles (Gem@rPPY) to enhance the therapeutic efficacy against TNBC. We demonstrate the outstanding photothermal capacity of Gem@rPPY under NIR irradiation, promoting the production of reactive oxygen species (ROS) and inducing local thermal effects. Through *in vitro* and *in vivo* experiments, we establish the remarkable tumor suppression capabilities of Gem@rPPY, highlighting its potential as a dual-action therapeutic strategy for TNBC. The current study shed light on the potential of engineering the surface roughness in superior chemophotothermal combination therapy against TNBC.

2. Materials and methods

2.1 Synthesis of rPPY, Gem@rPPY, PPY, and Gem@PPY

For the preparation of rPPY, dissolve 40.0 mg of pluronic P123 (Sigma-Aldrich, USA) in 8.0 mL of deionized water and stir vigorously overnight to form a uniform and transparent P123 aqueous solution. Next, add 60.0 μL of pyrrole monomer to the solution, then stir at an appropriate speed in a constant-temperature water bath at 40 °C for 1 hour. Initiate the polymerization process by adding 120.0 mg of ammonium persulfate, and after 4 hours of reaction, separate rPPY by centrifugation, followed by washing with ethanol and deionized water three times. The preparation of Gem@rPPY was carried out by first adding gemcitabine to the rPPY solution, followed by stirring for 24 hours and subsequent lyophilization using a vacuum freeze dryer. For the synthesis of PPY, dissolve 1.32 g polyvinyl alcohol (PVA, MW 31000, Aldrich) in 400 mL distilled water under high-speed stirring for 30 minutes. Next, add 29.9 g (184 mmol) of ferric chloride (Aldrich) to the solution and stir at 350 rpm for 1 hour to form a PVA/ferric chloride solution. Subsequently, under continuous stirring, slowly add 2.55 g (38 mmol) of recently distilled pyrrole (Aldrich) to the solution. After 2 hours of polymerization reaction, collect the solid product by centrifugation, wash it multiple times with distilled water, then re-disperse it in water, and finally remove it by

freeze-drying to obtain PPY. Gem@PPY was prepared using the same procedure as Gem@rPPY, except that PPY was used as the carrier.

2.2 Drug loading and releasing assay

Prepare solutions of different concentrations of gemcitabine, test absorbance at 269 nm, and draw standard curves. Take 10.0 mg of gemcitabine and 5.0 mL of rPPY and PPY, stir for 24 hours. Centrifuge and clean 3 times, collect 20.0 mL of supernatant, dilute 1.0 mL of supernatant to 5.0 mL each, measure absorbance at 269 nm, calculate the concentration of supernatant based on absorbance and standard curve. For drug release assay, add 2.0 mL of Gem@rPPY and Gem@PPY concentrate to 0.4 mL and add 3.6 mL of PBS with different pH values (pH = 7.4/6.0/5.0) for drug release behavior analysis. Set the sampling times at 1, 2, 4, 8, 12, 24, and 48 hours, measure the absorbance of the supernatant at 269 nm after centrifugation of 0.2 mL each time. Then add 0.2 mL of PBS with different pH values and continue to incubate until 48 hours to test the drug release curve.

2.3 Characterizations

The transmission electron microscope (TEM, JEOL JEM-F200, Japan) operating at an accelerating voltage of 200 kV was employed for imaging Gem@rPPY and rPPY. The drug loading property was assessed and quantified using Fourier Transform Infrared spectrometer (FT-IR, Thermo Scientific Nicolet iS5, USA). Zeta potentials alterations between Gem@rPPY and rPPY were measured utilizing Malvern Zetasizer Nano-ZS. For the determination of optimal treatment parameters, 1.0 mL of Gem@rPPY at a concentration of 1 mg mL^{-1} was separately introduced into 1.5 mL EP tubes and subjected to 808 nm laser irradiation at various powers (0.5, 1.0, 1.5, and 2.0 W cm^{-2}) until reaching their respective temperature peaks. Subsequently, photothermal conversion stability was evaluated through repeated irradiation and cooling cycles, and these *in vitro* photothermal characteristics were recorded using an Infrared Thermal Imager (Uti320E, UNI-T, China).

2.4 Cell culture

The murine mammary cancer cell line, 4T1, was procured from the American Type Culture Collection (ATCC, USA). Cells were cultured in a complete medium, comprising DMEM (Gibco, C11995500BT, USA), 10% fetal bovine serum (Gibco, 10099-141C, USA), and 1% Penicillin-Streptomycin solution (Beyotime, C0222, China). Prior to experimentation, the cells were cultured at 37 °C in a humidified atmosphere with 5% CO$_2$. Cell quantification was performed using an automatic cell counter.

2.5 TNBC mouse model and evaluating *in vivo* anticancer effectiveness

Healthy female BALB/c mice (5~6 weeks old) were procured from the Animal Experiment Center of Army Medical University (Chongqing, China). All animal experiments were carried out according to the ethical standards outlined in the 'Laboratory Animal-Guideline for Ethical Review of Animal Welfare' as per

the People's Republic of China National Standard (GB/T 35892-2018) and approved by the Animal Welfare and Ethics Committee of Army Medical University. The mice were housed in the specific pathogen-free (SPF) experiment center of Xinan Hospital with free access to water and food, following a 12 hour dark/light cycle. After a week of acclimatization, TNBC mouse models were induced by inoculating 1.0×10^6 prepared 4T1 cells into the right breast fat pad. One week later, mice with a tumor volume of 100–120 mm^3 were assigned to different groups ($n = 3$). Various materials (200.0 μL saline, 1.0 mg mL^{-1} rPPY (10 mg kg^{-1}), 0.3 mg mL^{-1} Gem@rPPY (3.0 mg kg^{-1}), and 1.0 mg mL^{-1} Gem@rPPY (10 mg kg^{-1})) were injected into the tail vein every two days until day 15 or until the tumor vanished. After 24 hours, 808 nm laser irradiation (1.5 W cm^{-2}) was applied to the tumor sites for 5 minutes, with manual temperature control around 45~50 °C. Subcutaneous tumor length and width were measured with vernier calipers every two days from day 0 to day 15, and tumor volume was calculated using the formula $V = (\text{length}) \times (\text{width})^2 \times 0.5$. Mice were weighed every other day, and on days 8 and 15, after painless anesthesia and sacrifice, tumors were collected, fixed with 4% paraformaldehyde, embedded in paraffin, and sectioned into 4 μm slices. Paraffin sections were used for subsequent Hematoxylin and Eosin (H&E) or immunohistochemical staining. The *in vivo* anticancer efficacy was evaluated by the ratio V/V_0, representing tumor volume at a given time compared to the initial volume.

2.6 Tumor aggression and biodistribution assessments

The assessment of Gem@rPPY tumor aggregation and *in vivo* photothermal efficacy was conducted by intravenously injecting different groups of mice with 200.0 μL saline, 0.3 mg mL^{-1} Cy5.5 labeled Gem@rPPY, 1 mg mL^{-1} Cy5.5 labeled Gem@rPPY, and rPPY. Following a 24 hour period, the mice were anesthetized, and subcutaneous images were captured using the Infrared Thermal Imager (Uti320E, UNI-T, China). Subsequently, mice were euthanized in a painless manner, and their hearts, livers, spleens, lungs, kidneys, and tumors were collected for an in-depth exploration of Gem@rPPY *in vivo* distribution through the utilization of *in Vivo* Imaging Systems (IVIS, AniView100).

2.7 Live/dead imaging

The investigation into Gem@rPPY's efficacy in eliminating TNBC cells *in vitro* involved Live–dead staining using the Calcein-AM and propidium iodide (PI) kit (BB-41262, Bestbio, China). 4T1 cells were separately incubated with 0.3, 0.7, and 1.0 mg mL^{-1} of Gem@rPPY for 12 hours, followed by 808 nm laser irradiation (1.5 W cm^{-2}, 3 min) and an additional 12 hour incubation period. Subsequently, the treated 4T1 cells were stained with Calcein-AM and PI, and images were recorded using a laser confocal microscope (ZISS880, Zeiss, Germany).

2.8 Trypan blue staining

Trypan blue staining was employed for *in vitro* assessment of Gem@rPPY's capability to induce apoptosis in TNBC. The protocol involved using Trypan blue (Solarbio, C0040) staining,

with the positive control group established using a Cell Apoptosis Induction Kit (C0006S, Beyotime, China) and the negative control group with a Programmed Cell Necrosis Induction Kit (C1058S, Beyotime, China). Following incubation with 1 mg mL^{-1} Gem@rPPY for 12 hours and exposure to 808 nm, 20.0 μL of 0.4% (W/V) Trypan blue solution was added to the wells and incubated for 5 minutes at room temperature. Subsequently, bright-field images were captured using an optical microscope (AxioObserver A1, Carl Zeiss, Germany).

2.9 Flow cytometry

We also performed flow cytometry after collecting the treated cells. The treated cells were collected and subjected to a series of steps. Initially, 4T1 cells were washed three times with PBS and subsequently stained with Anti-annexin V-FITC (1062M, Beyotime, China) and PI (1062 M, Beyotime, China) for 15 minutes in the dark. The fluorescence signals of FITC and PI were then meticulously recorded using the FACS Calibur flow cytometer (BD Biosciences, USA), with emission wavelengths of 515 nm and 560 nm, respectively.

2.10 Immunohistochemical staining

The expression of apoptosis-related proteins, namely Bcl-2-associated X protein (BAX), B-cell lymphoma-2 (BCL-2), heat shock protein 70 (HSP 70), caspase-3, and cleaved caspase-3, was investigated through immunohistochemical staining. The procedure involved antigen retrieval on dewaxed paraffin sections, followed by treatment with an endogenous peroxidase blocker (PV-9000, Zsbio, China) for 10 minutes at room temperature. After three washes with PBS, the sections were incubated with 100.0 μL of the primary antibody for 60 minutes, followed by additional PBS washes. A 100 μL reaction enhancer was applied and co-incubated for 20 minutes, followed by washing and subsequent incubation with 100.0 μL enhanced enzyme-labeled goat anti-mouse/rabbit IgG polymer (PV-9000, Zsbio, China) for 20 minutes. Further washes with PBS preceded the addition of Diaminobenzidine (DAB) chromogen for 6 minutes. After water rinsing, hematoxylin staining solution was applied for 20 seconds, followed by differentiation and a blue wash. Specific information regarding the primary antibodies used is as follows: BAX (AF0120, Affinity), BCL-2 (AF6139, Affinity), HSP70 (BF8277, Affinity).

2.11 Cell counting kit-8 (CCK-8) assay

To assess the *in vitro* toxicity of rPPY, 4T1 cells were seeded into 96-well plates and incubated overnight. Subsequently, different material groups (saline, 0.15, 0.3, 0.75, 1.0, 2.0, 4.0 and 10.0 mg mL^{-1} rPPY) were added, and co-cultured for 24 hours. After an additional 24 hour incubation and a gentle PBS wash, each well received freshly prepared CCK8 (CK04, Dojindo, Japan) working solution (100.0 μL DMEM plus 900.0 μL CCK8 reagent) and incubated for 3 hours. Following the reaction, the plate was measured using the SpectraMax M5 microplate reader to determine absorbance at 480 nm. Cell viability was then calculated by comparing the absorbance of cells subjected to various treatments with that of the control group.

2.12 Histological examination

Healthy BALB/c mice were randomly assigned to four groups ($n = 5$) and intravenously administered with either saline, rPPY, Gem@rPPY (with or without irradiation). On day 15, after anesthesia, vital organs, including hearts, livers, spleens, lungs, and kidneys, were excised, fixed with 4% paraformaldehyde, embedded in paraffin, and sectioned for subsequent H&E staining.

2.13 Statistics analysis

All results were expressed as the mean ± SD from a minimum of three independent experiments. Comparative analyses of relative expression values between two groups were conducted using the independent-samples *t*-test and SPSS 22.0 (SPSS, Inc., Chicago, IL, USA). For multiple groups, statistical analyses were performed using one-way ANOVA (GraphPad Prism 9.0). A threshold of $p < 0.05$ was considered statistically significant.

3. Results and discussion

3.1 Characterization of rPPY and Gem@rPPY

As shown in Fig. 1A, SEM imaging revealed the morphological features of the Pluronic P123-assisted synthesis of rPPY and conventional PPY nanoparticles assisted by PVA. It is interesting
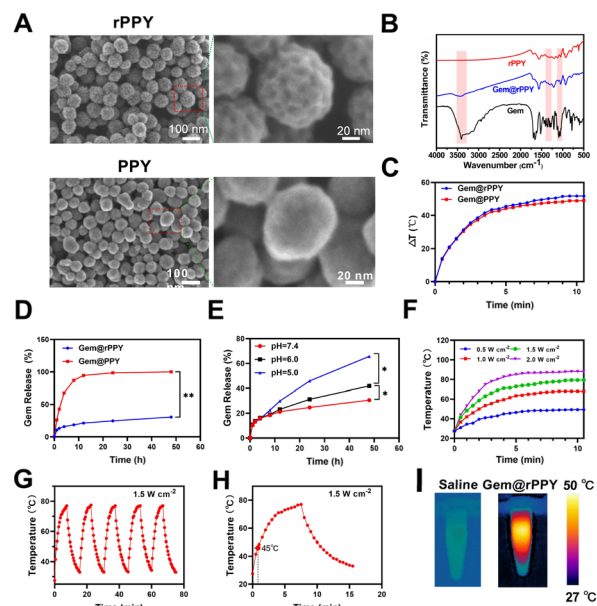

Fig. 1 (A) SEM image of rPPY and PPY. (B) Infrared spectrogram of Gem, rPPY and Gem@rPPY. (C) Temperature elevation curves of Gem@rPPY and Gem@PPY upon 808 nm laser irradiation at a power density of 1.5 W cm^{-2}. The concentrations of Gem@rPPY and Gem@PPY are both 1.0 mg mL^{-1}. (D) Time-course drug release profiles of Gem@rPPY and Gem@PPY. (E) Time-course drug release profiles of Gem@rPPY at different pH values. (F) Temperature over time curves of Gem@rPPY (1.0 mg mL^{-1}) at different power intensities (0.5, 1.0, 1.5, and 2.0 W cm^{-2}). (G–I) Photothermal conversion efficiency and thermal stability of Gem@rPPY at 1.5 W cm^{-2}. Data are presented as the means ± SD ($n = 3$). Statistical analysis was performed by one-way ANOVA analysis. *$P < 0.05$, **$P < 0.01$.

that the P123-templated rPPY exhibits a very rough surface with bulges around 3 nm, while PVA templated PPY display smooth surface. Further TEM characterization (Fig. S1†) indicated that rPPY does not have a mesoporous structure but instead has a high degree of surface roughness. Statistical analysis indicated an approximate particle size of 68.0 ± 9.0 nm was obtained for rPPY. P123 is a block copolymer composed of alternating hydrophilic ethylene oxide (PEO) and hydrophobic propylene oxide (PPO). This unique chemical structure endows P123 with excellent micelle formation ability and template action. In solution, P123 molecules will form a micelle structure, where the PPO portion forms a hydrophobic core facing inward and the PEO portion forms a hydrophilic shell facing outward. It was reported that silicon source materials (such as silane precursors) will interact with P123 during the curing process, allowing for the formation of mesoporous structures. Similarly, we reasoned that during the PPY formation, P123 formed small micelles around the nanoparticle surface. When P123 is removed in subsequent steps, the position of the original P123 micelles will become small pits and cavities. Nevertheless, the detailed molecular mechanism and chemical processes need further study.

It is well-documented that PPY nanoparticles are excellent photothermal agents and drug delivery carriers. We thus investigated if rPPY's unique surface morphology played a critical role in its properties as nanomedicines. First, Gemcitabine was loaded onto rPPY using the lyophilization method. FT-IR analysis in Fig. 1B was conducted to validate drug loading, confirming the presence of Gemcitabine in rPPY. The Gemcitabine loading efficiencies by rPPY and PPY were determined to be 10.11% and 2.18%, respectively. TEM results suggest that the morphology of Gem@rPPY didn't alter much after Gemcitabine loading (Fig. S2†). We then evaluated the photothermal properties of Gem@rPPY and Gem@PPY (Fig. 1C). It was found that Gem@rPPY displayed better photothermal performance than Gem@PPY. Drug releasing assay indicated that Gem@rPPY had a much slower Gemcitabine releasing profile (Fig. 1D). We also evaluated the release rate of gemcitabine from Gem@rPPY under different temperatures and media conditions. The drug release results indicate that the release rate is directly proportional to temperature (Fig. S3B†). In addition, the drug release rate in serum is lower than that in PBS (Fig. S3B†). Next, we examined the drug releasing behaviors of Gem@rPPY at different pH values (Fig. 1E). It was found that the release of Gemcitabine increased with lower pH values at the same time periods, as expected. As depicted in Fig. 1F, exposure to varying powers of 808 nm laser irradiation demonstrated that 1 mg mL^{-1} Gem@rPPY achieved its peak temperature within a remarkable 3 minutes, highlighting its superior photothermal conversion efficiency. Furthermore, as Fig. 1G–I suggested, it could be observed that the sustained capability of Gem@rPPY to attain temperatures between 45–50 °C within approximately 1 minute, even after repeated thermal cycles, underscored its exceptional photothermal stability, a crucial attribute for efficient cancer cell ablation. The abovementioned results suggested rPPY nanoparticles indeed exhibited improved photothermal efficacy and drug loading capability. We reasoned

that such an improvement was attributed to the rough surface of rPPY. Collectively, the morphological characteristics and drug-loading capacity of Gem@rPPY suggest its potential as an effective therapeutic agent.

3.2 Biodistribution and photothermal properties of Gem@rPPY *in vivo*

The rigorous validation of Gem@rPPY's photothermal efficacy encompassed both *in vitro* and *in vivo* assessments, leading to the identification of an optimal therapeutic approach. In-depth investigations into the photothermal characteristics and tumor retention capabilities of Gem@rPPY were then conducted in a TNBC mice model. We first examined the time-course biodistribution of Gem@rPPY. Fig. 2A shows that the fluorescence intensity in the tumor was higher than that in other organs and tissues, and this intensity decreased over time. Within 24 hours, the fluorescence intensity of Gem@rPPY in the tumor remained consistently higher than in other organs and tissues and the fluorescence intensity of the tumor decreased to 4.6% at the 24 hours compared to the 3 hours. The EPR effect was further confirmed by the results shown in Fig. 2B and C, as the tumor exhibited the highest fluorescence intensity compared to other major organs, validating the influence of the permeability and
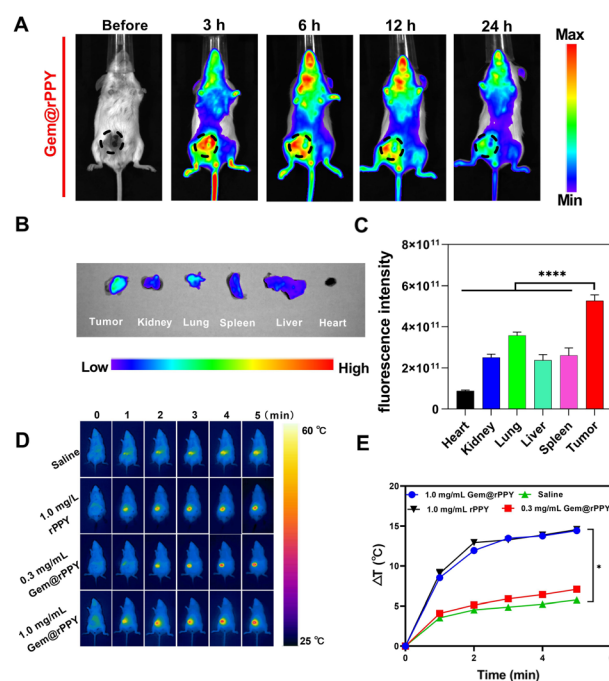

Fig. 2 (A) Representative fluorescence images of tumor-bearing mice treated with Gem@rPPY at various time points. (B) Biodistribution of Cy5.5-labeled Gem@rPPY in various mouse organs after tail-vein injection for 24 hours. (C) Semi-quantitative analysis of the accumulation of Gem@rPPY in different organs based on fluorescence intensity. (D) Thermal imaging of different groups in TNBC mice after 24 hours of tail vein injection. The dosages for rPPY were 1.0 mg mL^{-1} and Gem@rPPY were 0.3 and 1.0 mg mL^{-1}, respectively. (E) Temperature change curves for rPPY and Gem@rPPY at different dosages (1.5 W cm^{-2}, 5 min). Data are presented as the means $\pm$ SD ($n = 3$). Statistical analysis was performed by one-way ANOVA analysis. *$P < 0.05$, ****$P < 0.0001$.

retention (EPR) effect in promoting the accumulation and retention of Gem@rPPY in the tumor microenvironment.[44] Fig. 2D and E delineated the temporal temperature changes at the tumor site during *in vivo* experiments under laser irradiation. The unique enhanced EPR effect, characteristic of solid tumors, facilitated the accumulation of rPPY and Gem@rPPY in the tumor site *via* blood circulation. This accumulation, driven by defective vasculature and impaired lymphatic clearance, enabled Gem@rPPY to reach the requisite temperature for effective tumor cell eradication under laser irradiation. Notably, the temperature rise rate and peak value of Gem@rPPY were positively correlated with its concentration. These findings collectively underscore the promising therapeutic potential of Gem@rPPY for targeted and efficient photothermal therapy in TNBC.

3.3 Synergistic therapeutic effects of Gem@rPPY on TNBC

Following the successful induction of the TNBC mice model, Gem@rPPY was administered through tail vein injections every two days until day 15 (Fig. 3A). The study recorded tumor volumes and mouse weights, presenting intuitive photos of tumors in different groups on day 15 and a line graph illustrating tumor volume changes over time (Fig. 3B and C). The findings suggest a synergistic therapeutic effect of Gemcitabine and polypyrrole (with 808 nm) on TNBC tumors, supported by the roughed surface structure, with a positive correlation between efficacy and dosage. No significant differences were observed between the rPPY and saline groups. The 808 nm only group and the group treated with gemcitabine showed similar therapeutic effects. The curve of mouse body weight over time (Fig. 3D) suggested no evident side effects caused by Gem@rPPY. In addition, therapeutic efficacy was validated through *in vitro* cell experiments, revealing a significant increase in ROS fluorescence intensity in
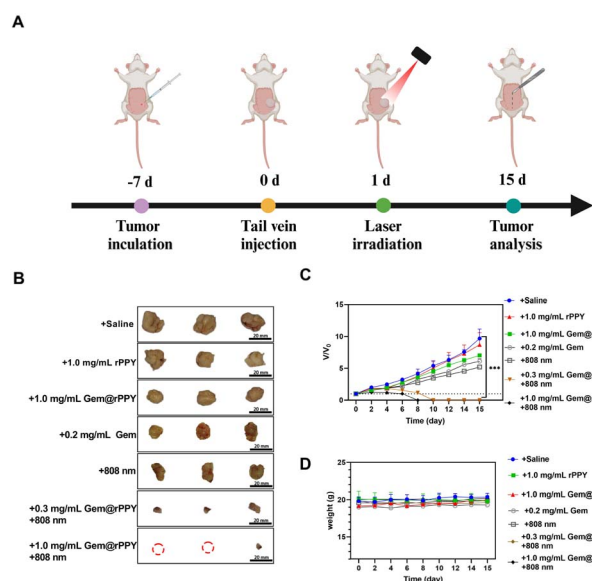

Fig. 3 (A) Establishment and treatment process of TNBC mice model. (B) Tumor photos of different groups in TNBC mice after 15 days of treatment. (C) Changes in tumor volume (D) changes in mice body weight. Data are presented as the means ± SD ($n = 3$). Statistical analysis was performed by one-way ANOVA analysis, ***$P < 0.01$.
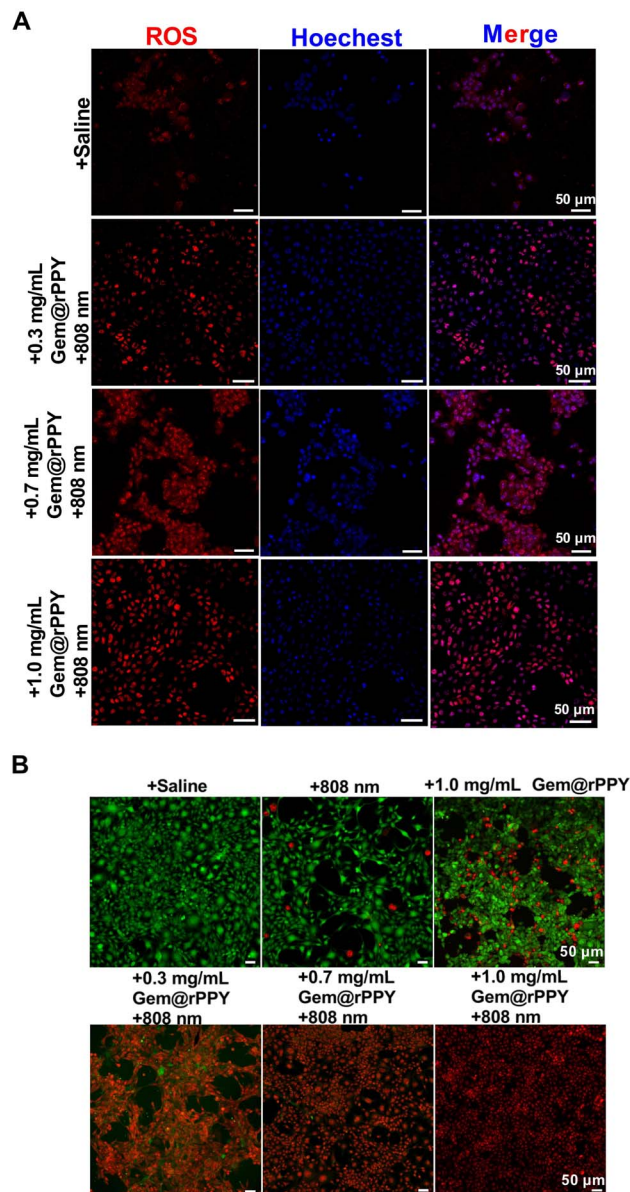

Fig. 4 (A) The confocal images of ROS in 4T1 cells before and after treatment with different concentrations of Gem@rPPY and laser irradiation. (B) The confocal images of Calcein-AM and PI staining (red: dead cells, green: live cells). The incubation time was 12 h.

the Gem@rPPY group, indicating the promotion of ROS production under heat stress (Fig. 4A and S4†). Further quantitative analysis using flow cytometry also indicates that the Gem@rPPY + 808 nm group displayed increased ROS levels in 4T1 cells (Fig. S5†). Live–Dead staining results (Fig. 4B) demonstrated the exceptionally high efficiency of Gem@rPPY in killing tumor cells under 808 nm laser irradiation.

3.4 Selective induction of apoptosis by Gem@rPPY

Apoptosis and necrosis represent divergent cell death mechanisms, with necrosis characterized by compromised cell membrane integrity, damaged cellular function, and the release of toxic substances. In contrast, apoptosis, an integral part of

the cell cycle, preserves cell membrane integrity, minimizing the leakage of cellular content and reducing damage to surrounding tissues, establishing it as a cleaner cell death pathway.[44,45] To discern whether Gem@rPPY induces necrosis or apoptosis, we employed trypan blue staining, flow cytometry, and immunohistochemical analyses. Gem@rPPY-treated cells, as depicted in Fig. 5A, maintained integrity and were unstained akin to the apoptosis group, while necrotic cells in the control group exhibited blue staining due to compromised cell membrane integrity. Flow cytometry results (Fig. 5B) revealed a substantial increase in apoptotic cells after Gem@rPPY + 808 nm treatment. Notably, Gem@rPPY and 808 nm groups also induced moderate cell apoptosis rates that could be attributed to the cytotoxicity of Gemcitabine and the photo-thermal effects of 808 nm laser irradiation, respectively. Quantitative analysis indicated that the apoptotic rate of Gem@rPPY+808 nm group was 3.62 and 2.52 times higher than Gem@rPPY and 808 nm groups, respectively (Fig. 5C). Evaluation of apoptosis-related proteins (BAX, BCL-2, HSP 70, caspase-3, and cleaved caspase-3) in Fig. 6A and B demonstrated significantly elevated BAX, HSP 70, caspase-3, and cleaved caspase-3 levels, coupled with decreased BCL-2 expression in the treatment group, indicating effective apoptosis induction by Gem@rPPY in 4T1 cells. *In vivo* experiments further corroborated these findings, with immunohistochemical staining in Fig. 6C revealing heightened BAX and HSP70 expression, reduced BCL-2, and H&E staining displaying characteristic apoptotic morphology, featuring rounded and detached cells with reduced volume and condensation. Gem@rPPY's capacity to selectively induce apoptosis positions it as a promising and cleaner therapeutic intervention.
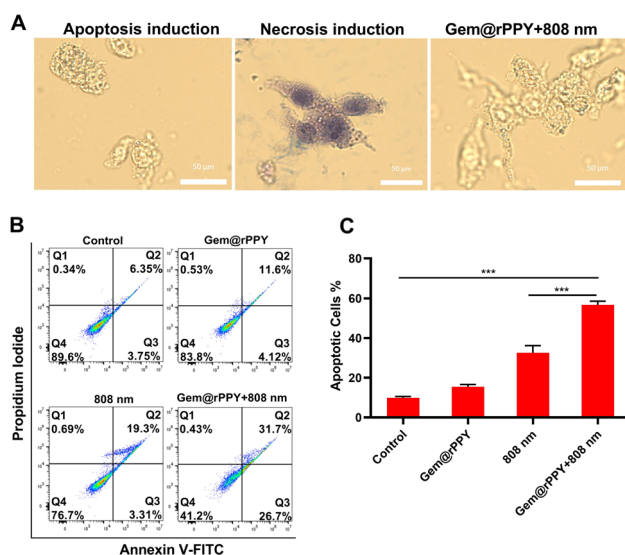

Fig. 5 (A) Bright field images of Gem@rPPY treated 4T1 cells stained with trypan blue, compared with apoptosis and necrosis groups. (B) Apoptotic proportion of 4T1 cells treated with Gem@rPPY (0.7 mg mL^{-1}) by flow cytometry. (C) Histogram of the apoptotic rate for different groups in (B). Data are presented as the means ± SD (n = 3). Statistical analysis was performed by one-way ANOVA analysis. *P < 0.05, **P < 0.01, ****P < 0.0001.
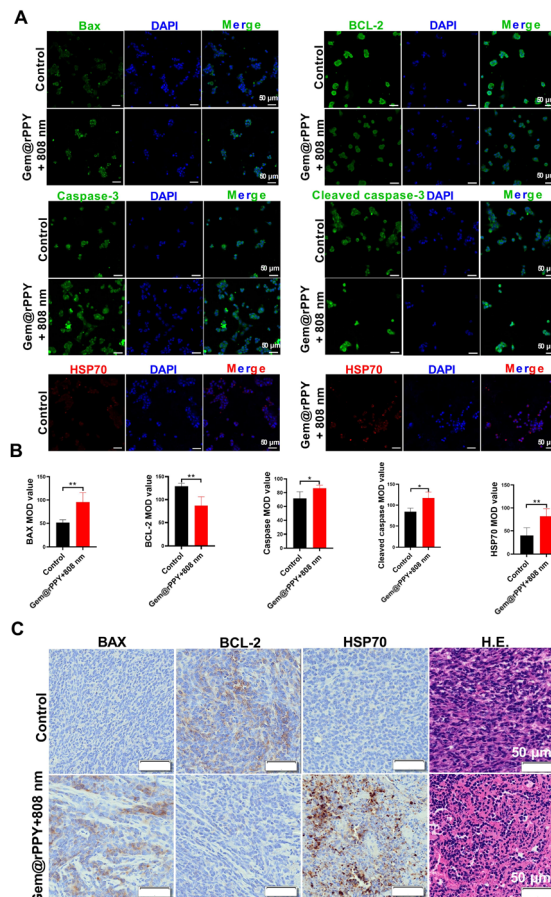

Fig. 6 (A) CLSM imaging of HSP70, BAX, BCL-2, cleaved caspase-3, and caspase-3 in 4T1 cells treated different sample formulations. (B) Semi-quantitative analysis of the fluorescence signals in (A). (C) Immunohistochemical staining of HSP70, Bax, and BCL-2 in tumor paraffin sections. Scale bar: 50 μM. Data are presented as the means ± SD (n = 3). Statistical analysis was performed by one-way ANOVA analysis. *P < 0.05, **P < 0.01, ****P < 0.0001.

3.5 Toxicity of rPPY and Gem@rPPY

To assess the toxicity of rPPY, we conducted *in vitro* experiments with eight concentration groups spanning low to high levels. As depicted in Fig. 7A, after co culturing with 4T1 cells, the survival of 4T1 cells was not significantly affected when the dosage of rPPY was below 1.0 mg mL^{-1}. When the dose concentration was increased to 4.0 mg mL^{-1}, the cell survival rate was about 50%. When the concentration was increased to 10.0 mg mL^{-1}, the cell survival rate decreased to nearly 20%. Fig. 7B displays the major organs removed from TNBC mice on day 15, and H&E staining indicated that Gem@rPPY exhibited excellent biocompatibility, paving the way for potential human applications.

3.6 Discussion

Breast cancer, particularly the aggressive TNBC subtype, presents a significant challenge in oncology due to its poor prognosis and limited treatment options.[46,47] Here, our study introduces a PPY nanoparticle with roughed surface structure. The roughness of rPPY was attributed to the use of a surfactant, P123, which forms
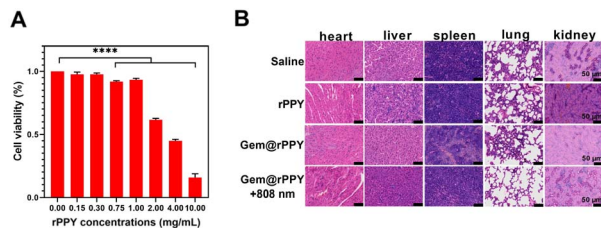
Fig. 7 (A) Cell viability of 4T1 cells co-incubated with different concentrations of rPPY. Incubation time was 24 h. (B) H&E staining of main organs and tumors in different groups of TNBC mice. The concentration of Gem@rPPY was 1.0 mg mL^{-1}. Scale bar: 50 μM. Data are presented as the means $\pm$ SD ($n = 5$). Statistical analysis was performed by one-way ANOVA analysis. ****$P < 0.0001$.

small micelles that eventually led to the cavities and pits on the rPPY surface. More importantly, such a rough PPY nanoparticle greatly enhanced the drug loading efficiency of the chemotherapeutic drug Gemcitabine and also improved the photothermal performance of rPPY, highlighting the potential benefits of this unique nanostructure in biomedical applications. The comprehensive characterization of Gem@rPPY confirms its successful synthesis, with SEM revealing well-defined surface morphology and efficient drug loading. The photothermal properties of Gem@rPPY are thoroughly investigated, demonstrating efficient conversion and stability under varying conditions. *In vivo* experiments in a TNBC mouse model establish the remarkable tumor suppression capabilities of Gem@rPPY. The synergistic therapeutic effects of gemcitabine and polypyrrole are evident, showcasing the potential of Gem@rPPY as an effective treatment strategy. The in-depth analysis includes the evaluation of tumor volumes, mouse weights, and *in vitro* cell experiments demonstrating increased reactive oxygen species (ROS) production and efficient tumor cell ablation. Taken together, the above-mentioned results suggest that surface-engineered Gem@rPPY is an excellent dual-action therapeutic strategy for TNBC therapy.

Conclusions

In conclusion, the current study constructed a Gem@rPPY nanoparticle with rough surfaces as a promising candidate for the combination therapy of TNBC. The rough surface enhanced the photothermal efficacy and drug loading efficiency of rPPY. Moreover, the synergistic effects of photothermal therapy and gemcitabine, coupled with the selective induction of apoptosis and excellent biocompatibility, position Gem@rPPY as a significant advancement in the quest for effective and targeted breast cancer therapies. The current study's findings open avenues for future research and clinical applications in the ongoing battle against TNBC.

Data availability

The datasets generated during and/or analysed during the current study are not publicly available but are available from the authors on reasonable request.

Author contributions

Yuanyin Xi: investigation, formal analysis, visualization, writing – original draft, data curation. Shiqi Zhou: investigation, writing – original draft, formal analysis. Junhui Long: conceptualization, supervision, resources. Linxi Zhou: methodology, visualization. Peng Tang: formal analysis, supervision. Hang Qian: conceptualization, writing – review &editing, supervision. Jun Jiang: conceptualization, supervision. Ying Hu: formal analysis, writing – original draft, supervision, funding acquisition.

Conflicts of interest

The authors declare no conflicts of interest.

Acknowledgements

Notes and references

1 C. DeSantis, J. Ma, L. Bryan and A. Jemal, *Ca-Cancer J. Clin.*, 2014, **64**, 52–62.
2 M. Yi, T. Li, M. Niu, S. Luo, Q. Chu and K. Wu, *Biomark. Res.*, 2021, **9**, 55.
3 F. Borri and A. Granaglia, *Semin. Cancer Biol.*, 2021, **72**, 136–145.
4 J. D. Brenton, L. A. Carey, A. A. Ahmed and C. Caldas, *J. Clin. Oncol.*, 2005, **23**, 7350–7360.
5 L. Carey, E. Winer, G. Viale, D. Cameron and L. Gianni, *Nat. Rev. Clin. Oncol.*, 2010, **7**, 683–692.
6 A. Goldhirsch, E. P. Winer, A. S. Coates, R. D. Gelber, M. Piccart-Gebhart, B. Thurlimann and H. J. Senn, *Ann. Oncol.*, 2013, **24**, 2206–2223.
7 T. C. Poteat, M. A. Adams, J. Malone, S. Geffen, N. Greene, M. Nodzenski, A. G. Lockhart, I. H. Su and L. T. Dean, *Cancer*, 2021, **127**, 3514–3522.
8 R. Dent, M. Trudeau, K. I. Pritchard, W. M. Hanna, H. K. Kahn, C. A. Sawka, L. A. Lickley, E. Rawlinson, P. Sun and S. A. Narod, *Clin. Cancer Res.*, 2007, **13**, 4429–4434.
9 C. Kang and Y. Y. Syed, *Drugs*, 2020, **80**, 601–607.
10 G. J. Morris, S. Naidu, A. K. Topham, F. Guiles, Y. Xu, P. McCue, G. F. Schwartz, P. K. Park, A. L. Rosenberg, K. Brill and E. P. Mitchell, *Cancer*, 2007, **110**, 876–884.
11 M. J. Duffy, P. M. McGowan and J. Crown, *Int. J. Cancer*, 2012, **131**, 2471–2477.
12 Y. Li, H. J. Zhang, Y. Merkher, L. Chen, L. Chen, N. Liu, S. Leonov and Y. H. Chen, *J. Hematol. Oncol.*, 2022, **15**, 121.
13 Q. Wu, W. Qian, X. L. Sun and S. J. Jiang, *J. Hematol. Oncol.*, 2022, **15**, 143.
14 H. N. Bell, R. J. Rebernick, J. Goyert, R. Singhal, M. Kuljanin, S. A. Kerk, W. Huang, N. K. Das, A. Andren, S. Solanki, S. L. Miller, P. K. Todd, E. R. Fearon, C. A. Lyssiotis, S. P. Gygi, J. D. Mancias and Y. M. Shah, *Cancer Cell*, 2022, **40**, 185–200.

15 D. S. Wei, Y. J. Yu, X. C. Zhang, Y. H. Wang, H. Chen, Y. Zhao, F. Y. Wang, G. H. Rong, W. W. Wang, X. Kang, J. Cai, Z. H. Wang, J. Y. Yin, M. Hanif, Y. B. Sun, G. F. Zha, L. X. Li, G. H. Nie and H. H. Xiao, *ACS Nano*, 2020, **14**, 16984–16996.

16 M. Chang, Z. Y. Hou, M. Wang, C. Z. Yang, R. F. Wang, F. Li, D. L. Liu, T. L. Peng, C. X. Li and J. Lin, *Angew Chem. Int. Ed. Engl.*, 2021, **60**, 12971–12979.

17 M. Y. Chang, M. Wang, M. F. Wang, M. M. Shu, B. B. Ding, C. X. Li, M. L. Pang, S. Z. Cui, Z. Y. Hou and J. Lin, *Adv. Mater.*, 2019, **31**, e1905271.

18 H. T. Yuan, P. Xia, X. Sun, J. B. Ma, X. L. Xu, C. J. Fu, H. C. Zhou, Y. D. Guan, Z. F. Li, S. S. Zhao, H. F. Wang, L. Y. Dai, C. C. Xu, S. H. Dong, Q. S. Geng, Z. J. Li and J. G. Wang, *Small*, 2022, **18**, e2202161.

19 A. D. Garg, A. M. Dudek, G. B. Ferreira, T. Verfaillie, P. Vandenabeele, D. V. Krysko, C. Mathieu and P. Agostinis, *Autophagy*, 2013, **9**, 1292–1307.

20 S. X. Chen, M. Ma, F. F. Xue, S. Z. Shen, Q. Chen, Y. C. Kuang, K. C. Liang, X. L. Wang and H. R. Chen, *J. Controlled Release*, 2020, **324**, 218–227.

21 H. Wang, R. Revia, K. Wang, R. J. Kant, Q. X. Mu, Z. Gai, K. L. Hong and M. Q. Zhang, *Adv. Mater.*, 2017, **29**, 1605416.

22 K. C. L. Black, J. Yi, J. G. Rivera, D. C. Z. Leon and P. B. Messersmith, *Nanomedicine*, 2013, **8**, 17–28.

23 W. Gao, Y. H. Sun, M. Cai, Y. J. Zhao, W. H. Cao, Z. H. Liu, G. W. Cui and B. Tang, *Nat. Commun.*, 2018, **9**, 231.

24 Y. Liu, B. M. Crawford and T. Vo-Dinh, *Immunotherapy*, 2018, **10**, 1175–1188.

25 H. K. Moon, S. H. Lee and H. C. Choi, *ACS Nano*, 2009, **3**, 3707–3713.

26 A. Sharma, V. Singh, T. L. Bougher and B. A. Cola, *Nat. Nanotechnol.*, 2015, **10**, 1027–1032.

27 W. J. Xu, J. M. Qian, G. H. Hou, A. Suo, Y. P. Wang, J. L. Wang, T. T. Sun, M. Yang, X. L. Wan and Y. Yao, *ACS Appl. Mater. Interfaces*, 2017, **9**, 36533–36547.

28 D. Jaque, L. M. Maestro, B. D. Rosal, P. H. Gonzalez, A. Benayas, J. L. Plaza, E. M. Rodríguez and J. G. Solé, *Nanoscale*, 2014, **6**, 9494–9530.

29 J. W. Kim, E. I. Galanzha, E. V. Shashkov, H. M. Moon and V. P. Zharov, *Nat. Nanotechnol.*, 2009, **4**, 688–694.

30 C. B. Leng, X. Zhang, F. X. Xu, Y. Yuan, H. Pei, Z. H. Sun, L. Li and Z. H. Bao, *Small*, 2018, **14**, e1703077.

31 J. W. Li, H. Xiao, S. J. Yoon, C. B. Liu, D. Matsuura, W. Y. Tai, L. Song, M. O'Donnell, D. Cheng and X. H. Gao, *Small*, 2016, **12**, 4690–4696.

32 T. Liu, M. K. Zhang, W. L. Liu, X. Zeng, X. L. Song, X. Q. Yang, X. Z. Zhang and J. Feng, *ACS Nano*, 2018, **12**, 3917–3927.

33 Z. Liu, H. Lin, M. L. Zhao, C. Dai, S. J. Zhang, W. J. Peng and Y. Chen, *Theranostics*, 2018, **8**, 1648–1664.

34 N. Lu, W. P. Fan, X. Yi, S. Wang, Z. T. Wang, R. Tian, O. Jacobson, Y. J. Liu, B. C. Yung, G. G. Zhang, Z. G. Teng, K. Yang, M. M. Zhang, G. Niu, G. M. Lu and X. Y. Chen, *ACS Nano*, 2018, **12**, 1580–1591.

35 X. J. Yu, A. Li, C. Z. Zhao, K. Yang, X. Y. Chen and W. W. Li, *ACS Nano*, 2017, **11**, 3990–4001.

36 D. Zhang, Y. S. Zheng, Z. G. Lin, S. Y. Lan, X. L. Zhang, A. X. Zheng, J. Li, G. Liu, H. H. Yang, X. L. Liu and J. F. Liu, *Small*, 2019, **15**, e1902636.

37 A. Ramanaviciene, W. Schuhmann and A. Ramanavicius, *Colloids Surf., B*, 2006, **48**, 159–166.

38 Z. B. Zha, Z. J. Deng, Y. Y. Li, C. H. Li, J. R. Wang, S. M. Wang, E. Z. Qu and Z. F. Dai, *Nanoscale*, 2013, **5**, 4462–4467.

39 L. Hao, C. Dong, L. Zhang, K. Zhu and D. Yu, *Polymers*, 2022, **14**(23), 5139.

40 X. Dai, X. Zhao, Y. Liu, B. Chen, X. Ding, N. Zhao and F. J. Xu, *Small*, 2021, **17**, e2006004.

41 Y. Xue, L. Zhang, F. Liu, Y. Zhao, J. Zhou, Y. Hou, H. Bao, L. Kong, F. Ma and Y. Han, *Adv. Healthcare Mater.*, 2022, **11**, e2200998.

42 G. Qian and J. Qiu, *Chem. Eng. J.*, 2019, **359**, 652–661.

43 Y. Tian, J. Zhang, S. Tang, L. Zhou and W. Yang, *Small*, 2016, **12**, 721–726.

44 A. Anand, V. Lalzawmliana and V. Kumar, *J. Mech. Behav. Biomed. Mater.*, 2019, **89**, 89–98.

45 W. Islam, T. Niidome and T. Sawa, *J. Pers. Med.*, 2022, **12**, 1964.

46 O. Cuvillier, G. Pirianov, B. Kleuser, P. G. Vanek, O. A. Coso, S. Gutkind and S. Spiegel, *Nature*, 1996, **381**, 800–803.

47 G. K. Gupta, A. L. Collier, D. Lee, R. A. Hoefer, V. Zheleva, L. L. S. V. Reesema, A. M. T. Tan, M. L. Guye, D. Z. Chang, J. S. Winston, B. Samli, R. J. Jansen, E. F. Petricoin, M. P. Goetz, H. D. Bear and A. H. Tang, *Cancers*, 2020, **12**, 2392.